Supplemental material:

Supplementary Table S1.

TABLE 1. COMPILATION OF P-WAVE INTERVAL VELOCITIES (VP) ADOPTED FOR TIME-DEPTH CONVERSION OF THE SEISMIC PROFILES

Units	Bally et al. (1986)	Barchi et al. (1998)	Scisciani & Montefalcone (2006)	Artoni (2013)	Bigi et al. (2011)	Bigi et al. (2013)	Scisciani et al. (2014)	Latorre et al. (2016)	Di Bucci et al. (2021)	Buttinelli et al. (2021)	This study
Pleistocene - Holocene	2400	2500	–	1500–2400	–	2000	3600	–	2.2	–	2100
Upper Pliocene	2400	2500	–	1500–3000	–	2100–2200	–	–	3.4	–	2200–2400
Lower Pliocene	2400	2500	–	1800–3000	–	2400–3000	3600	–	4	–	2500
Miocene turbidites	3600	4000	3600	2000–3600	3600	3100	4000	3900	4	4000	3200–3600
Eocene–Miocene marls	3400	4000	3600	2800–3500	4500	3200	4000	–	4.8	4800	4400
Scaglia Group	4500	–	4200	2800–3500	5800	–	5000	–	5.8	5800	4800
Lower Jurassic–Lower Cretaceous	5200	5500	5000	2800–3500	6100	5100	5500	–	5.9	5900	5100
Calcare Massiccio Fm.	6100	–	5500–6400	3600–4200	6400	5100	6800	5700	6.3	6400	5300
Anidriti di Burano Fm.	6300	6200	3900–5300	4200–5500	6040	–	6000	6300	6.3	6500	6300
Permo–Triassic metasediments	3900	5000	>3900	3900–6400	–	–	5500	5300	4.9	6500	5000
Crystalline Basement	–	–	–	–	–	–	6000	5800	–	–	5700

Note: published velocity values for the main stratigraphic units of the Umbria-Marche succession are compared with the interval velocities selected and refined in this study.

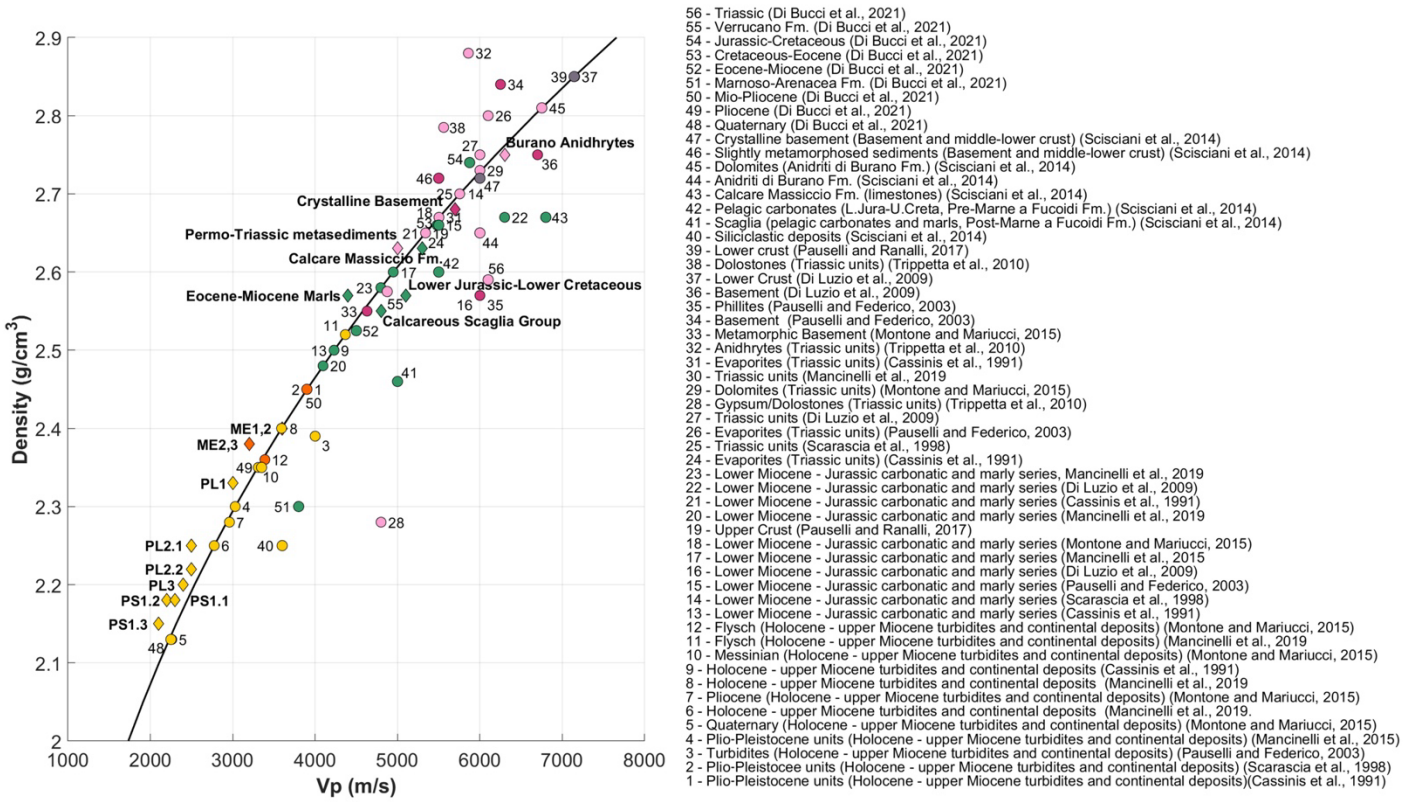

Figure S1. Comparative analysis of the densities and related Vp values assigned in this and previous studies to the main rock units of the Northern-Central Apennines. Black line: Relationship density/Vp according to the Gardner's rule. Circles: Previous studies; Diamonds: This study. Yellow: Pliocene-Pleistocene; Orange: Upper Miocene; Green: Jurassic-Lower Miocene; Pink: Triassic; Dark red: Crystalline-metamorphic basement; Dark Grey: Lower Crust. Densities for which previous authors didn't estimate Vp values were associated to values calculated by means of the Gardner's rule.

Supplemental Cross-sections.

Trace map of the cross sections used to construct the 3-D geological model and cross sections S1–S14.

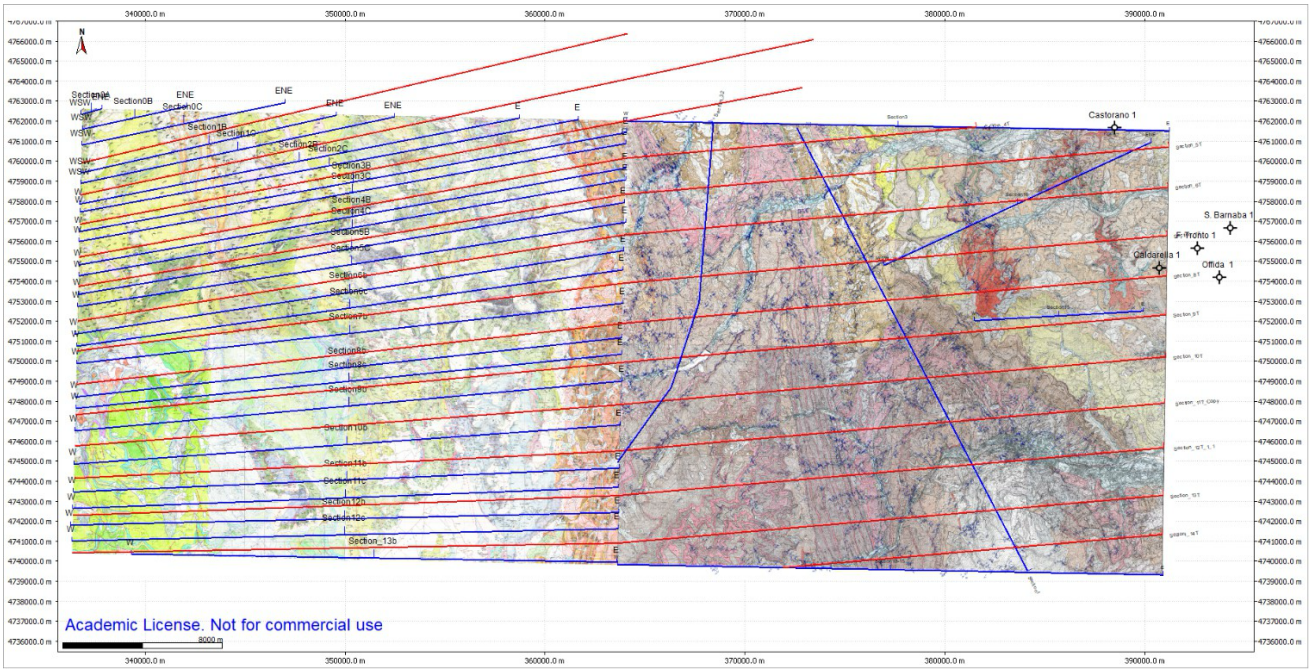

Figure S2. Trace map of the cross sections used to construct the 3-D geological model. Geological balanced cross sections S1–S14 are shown in red, and additional cross sections are shown in blue.

Figure S3. Cross section S1.

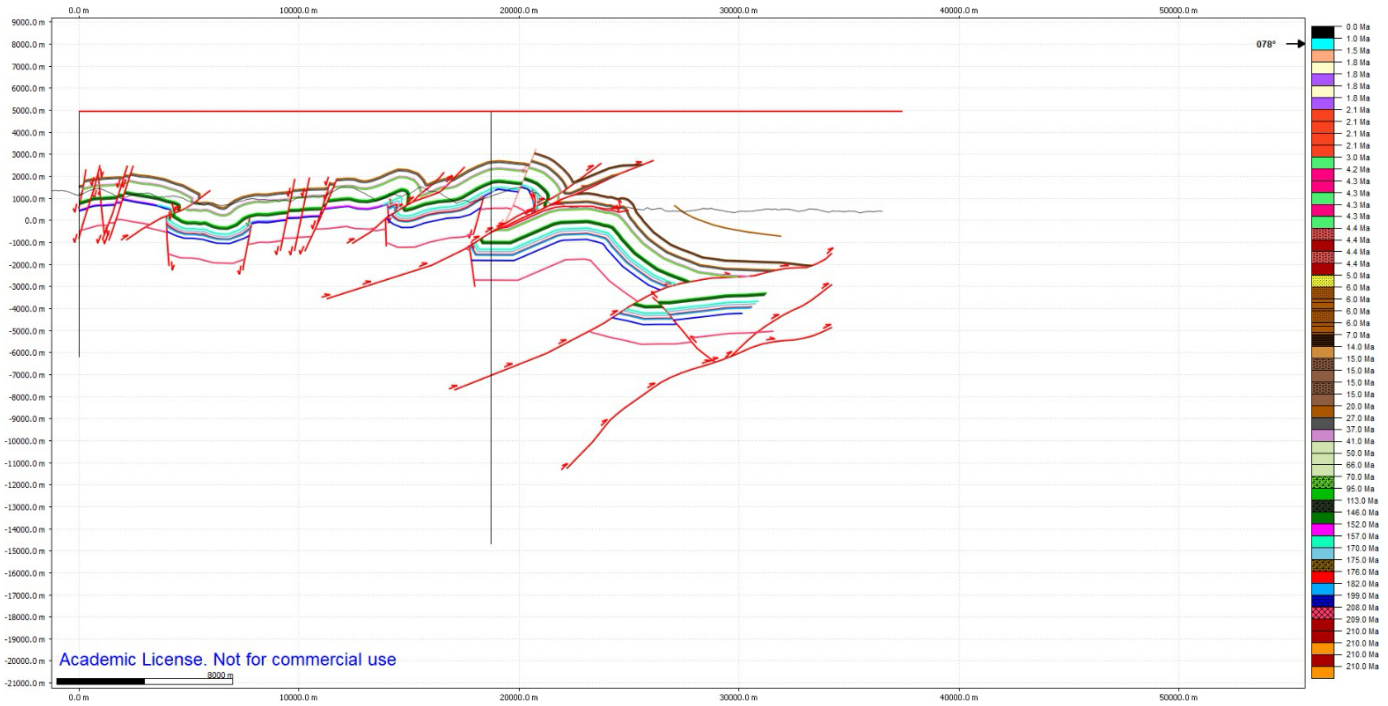

Figure S4. Cross section S2.

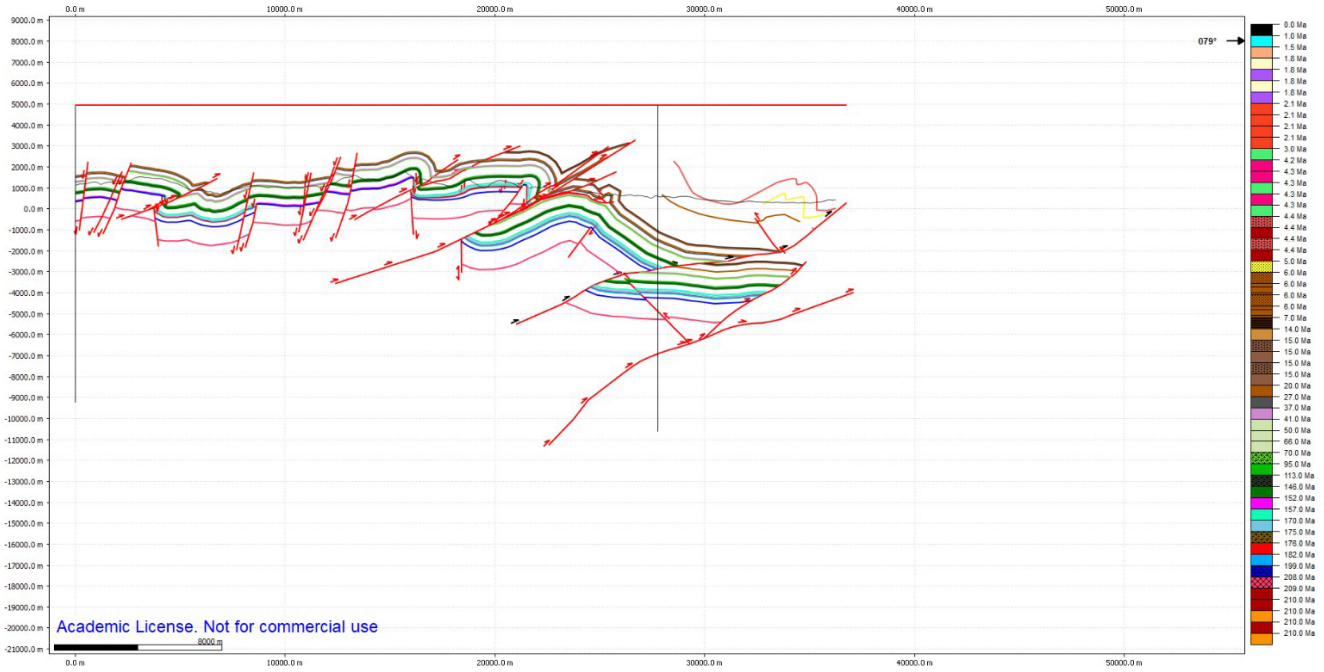

Figure S5. Cross section S3.

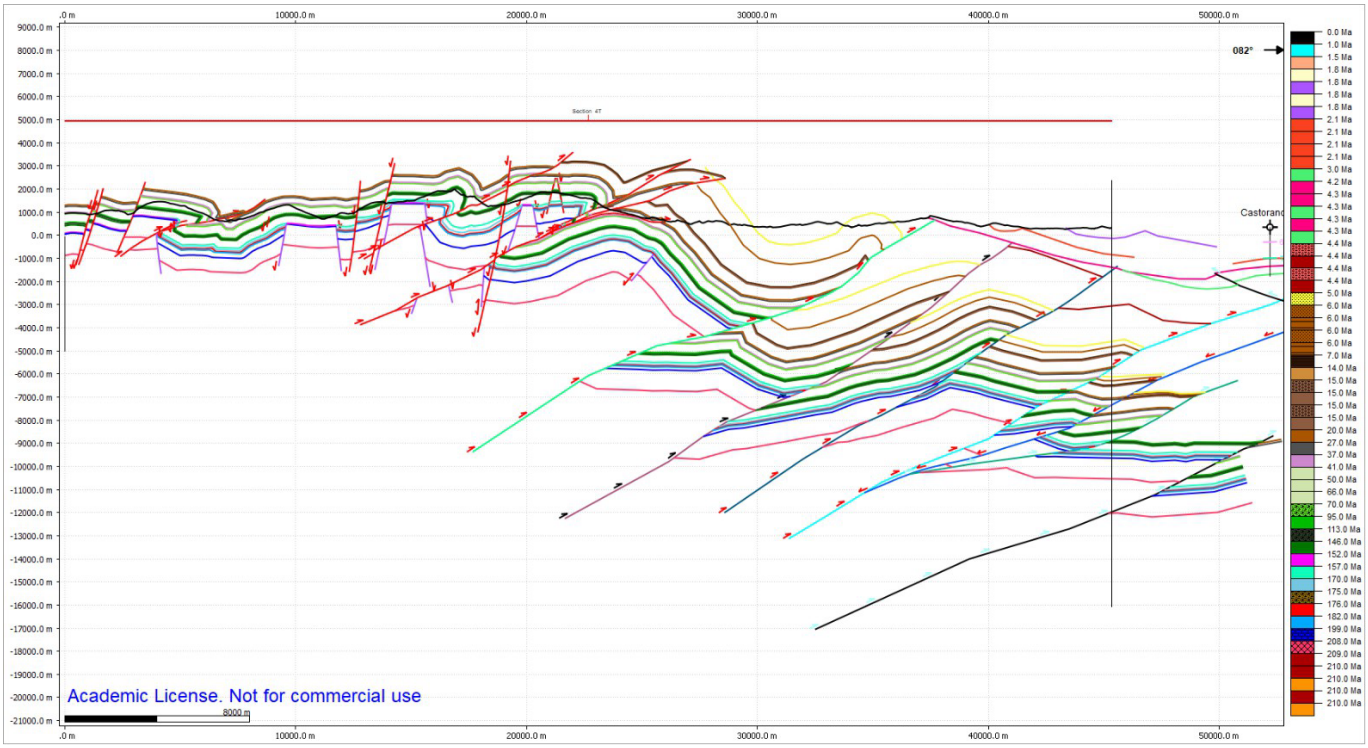

Figure S6. Cross section S4.

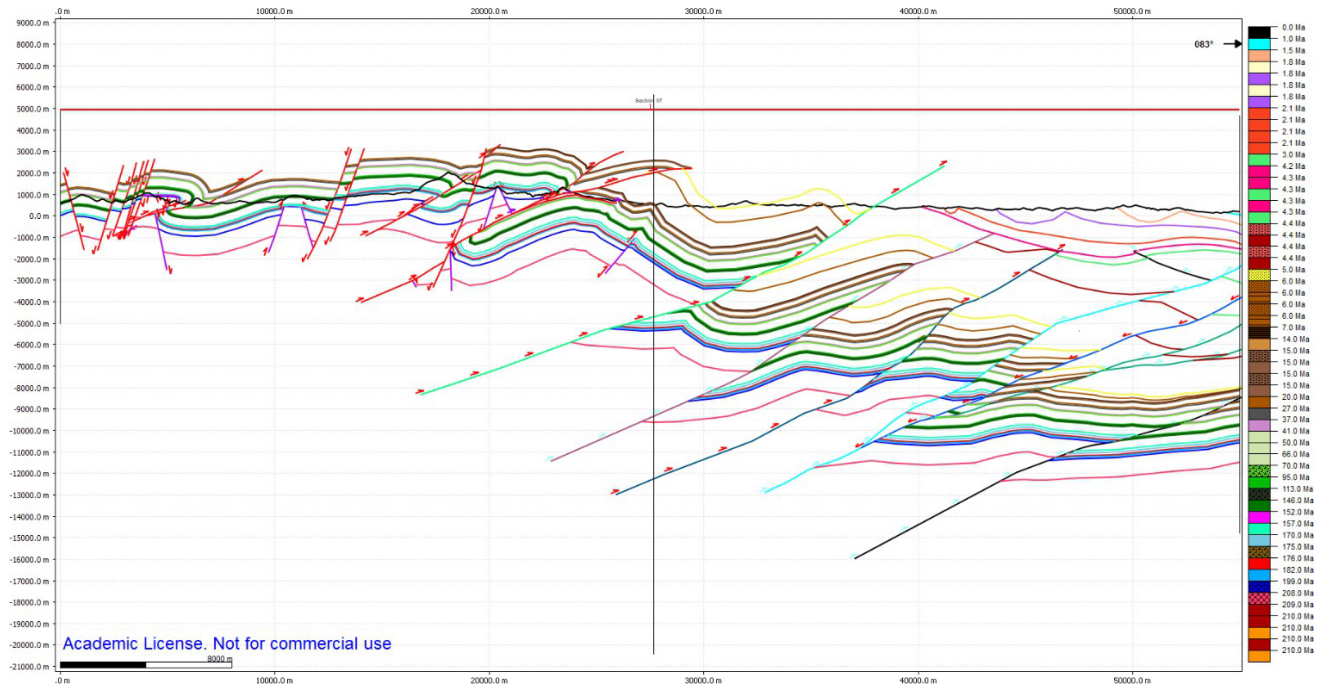

Figure S7. Cross section S5.

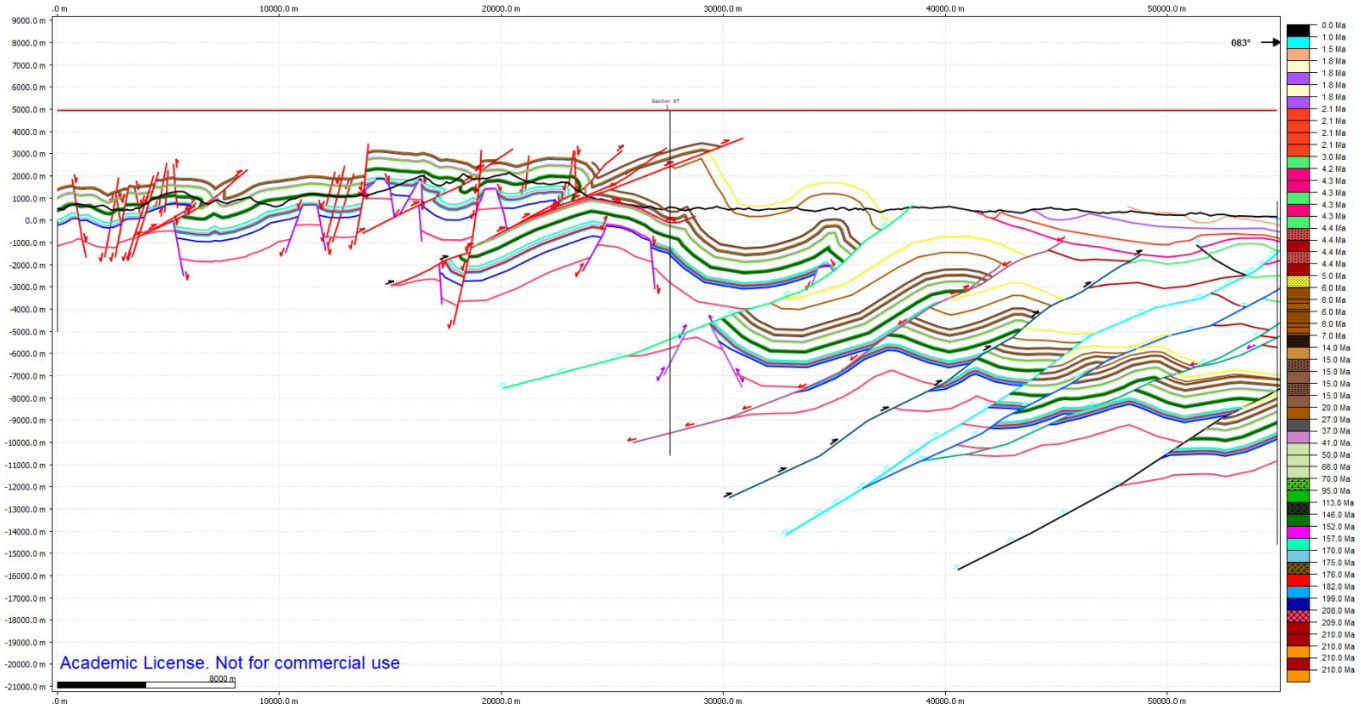

Figure S8. Cross section S6.

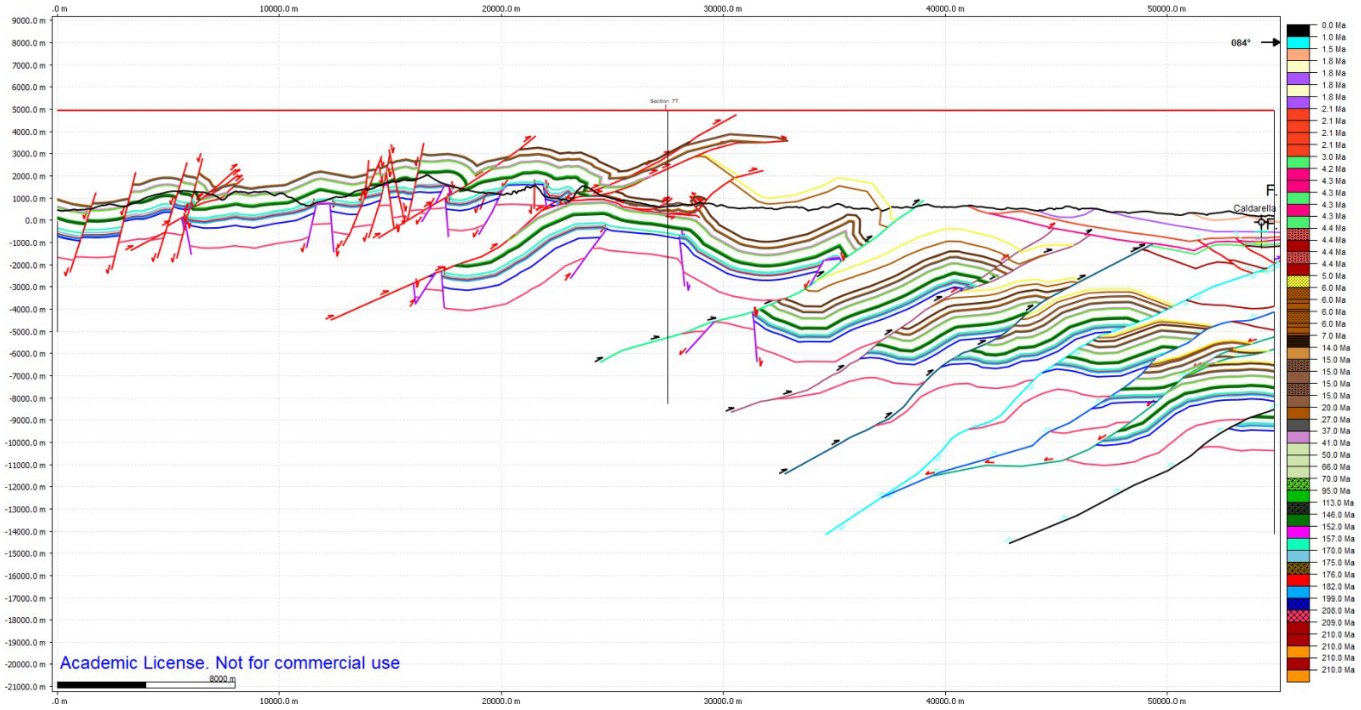

Figure S9. Cross section S7.

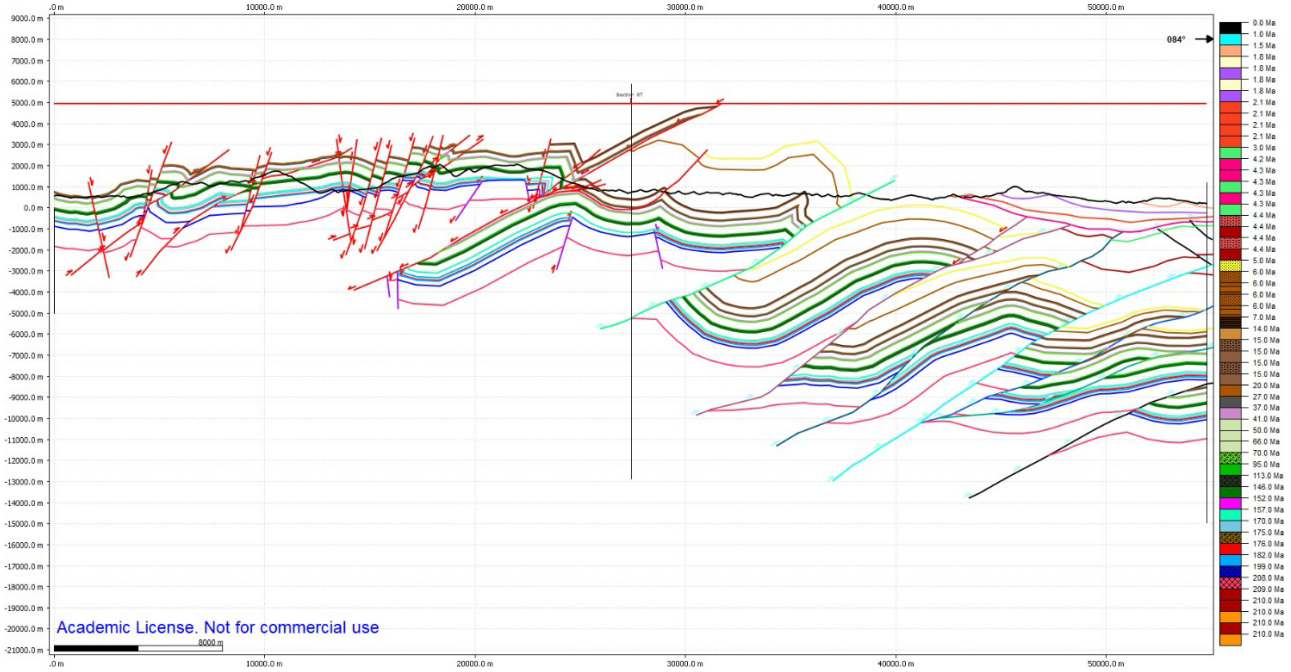

Figure S10. Cross section S8.

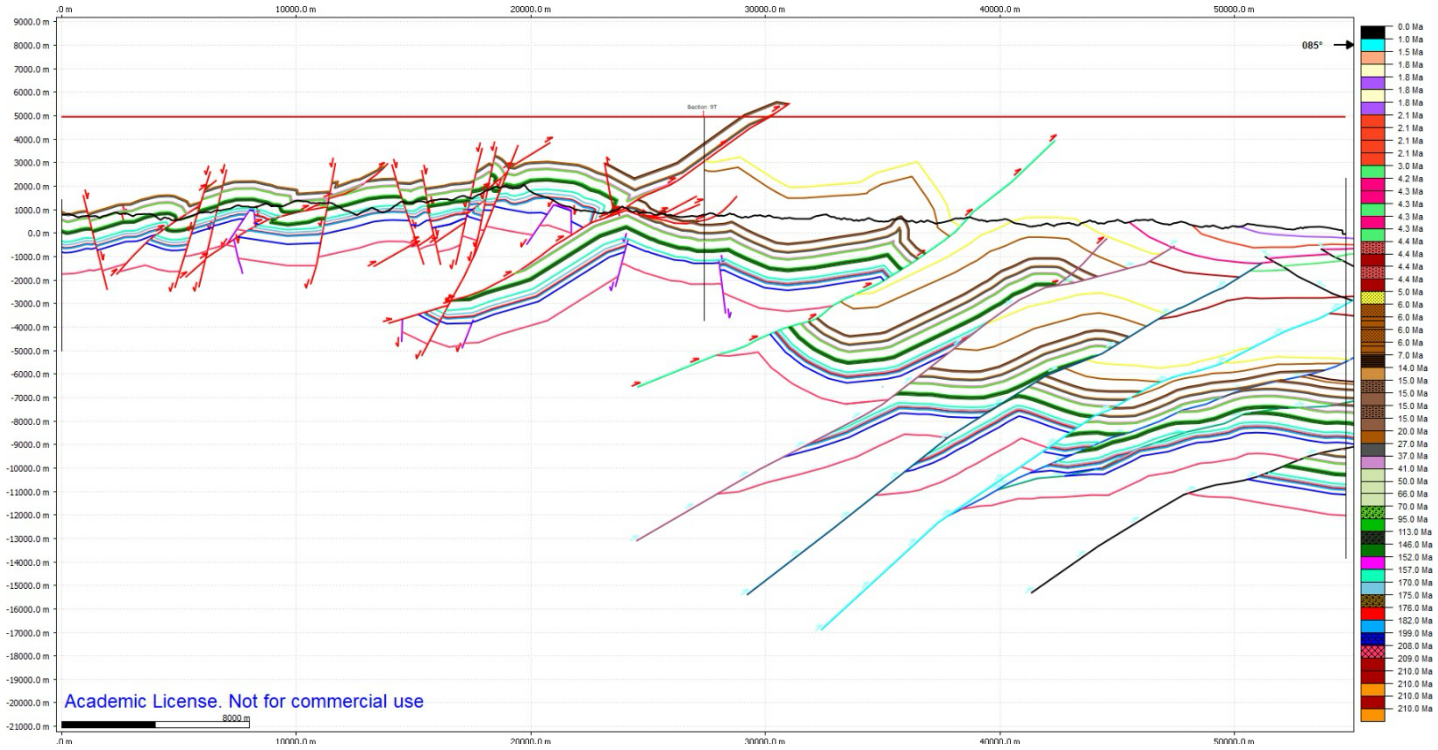

Figure S11. Cross section S9.

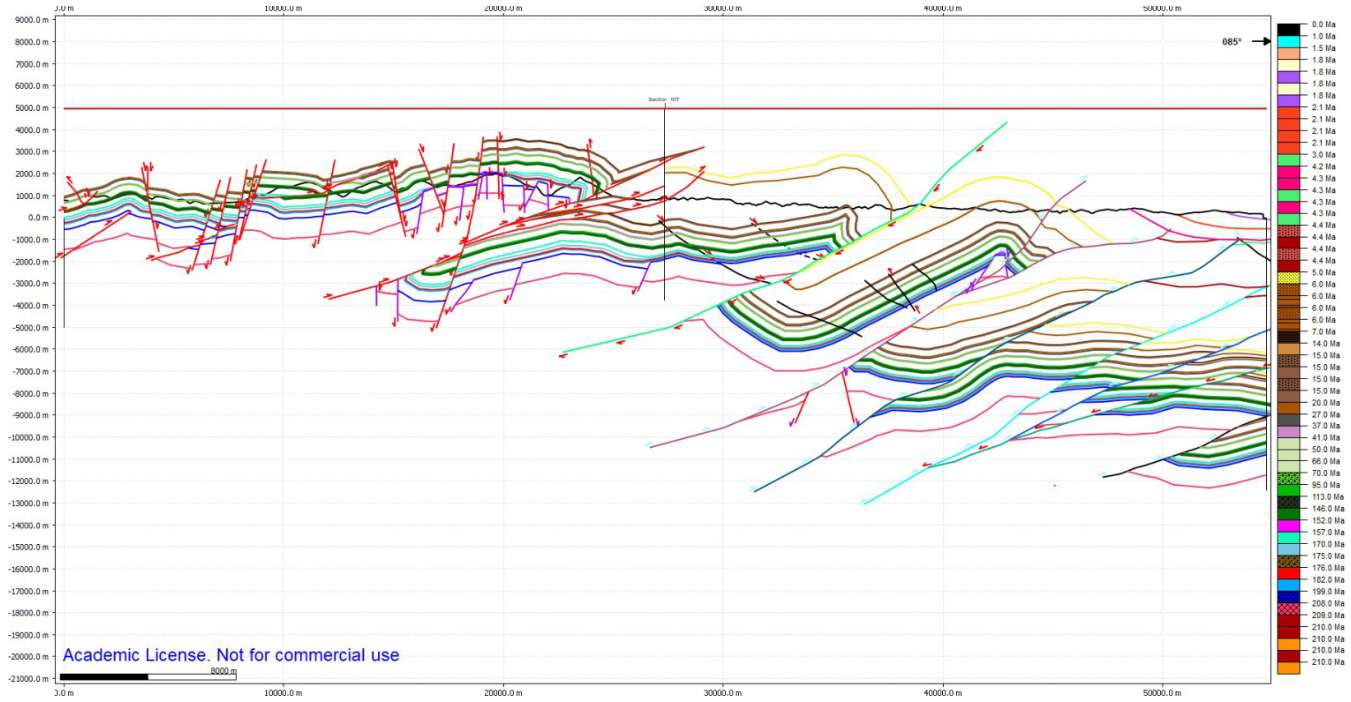

Figure S12. Cross section S10.

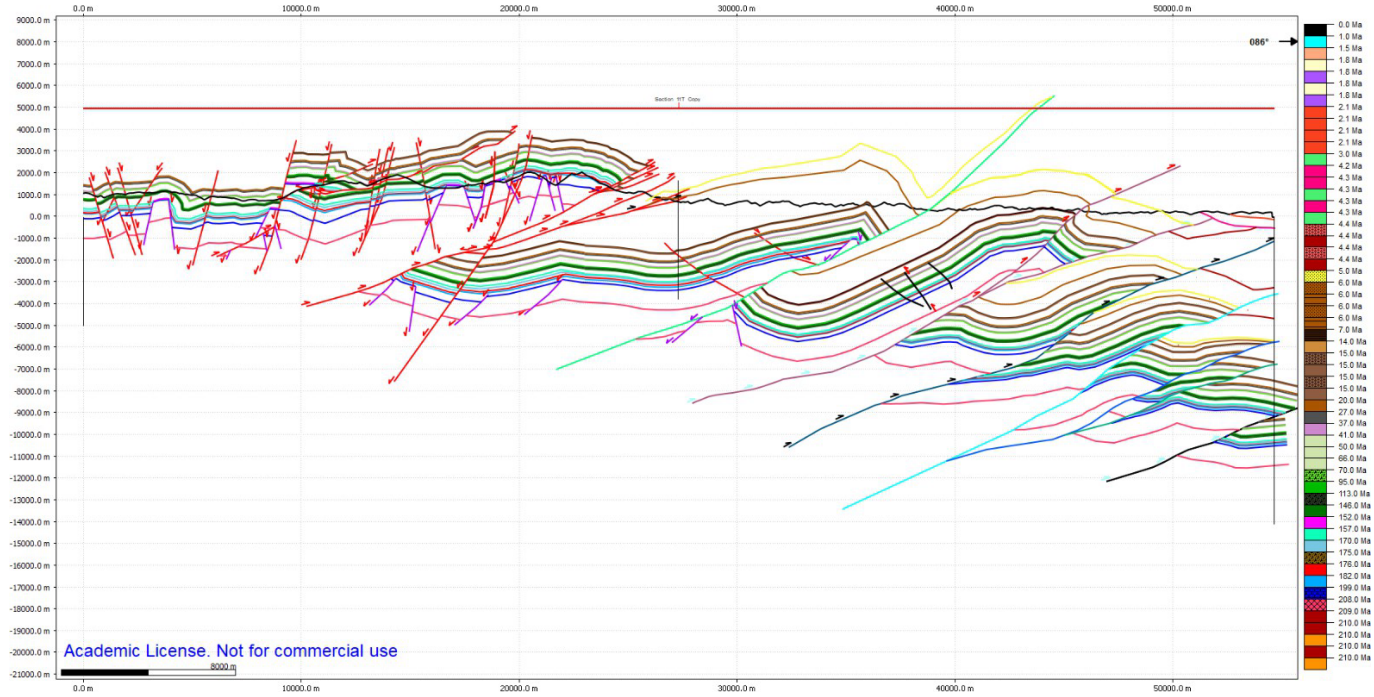

Figure S13. Cross section S11.

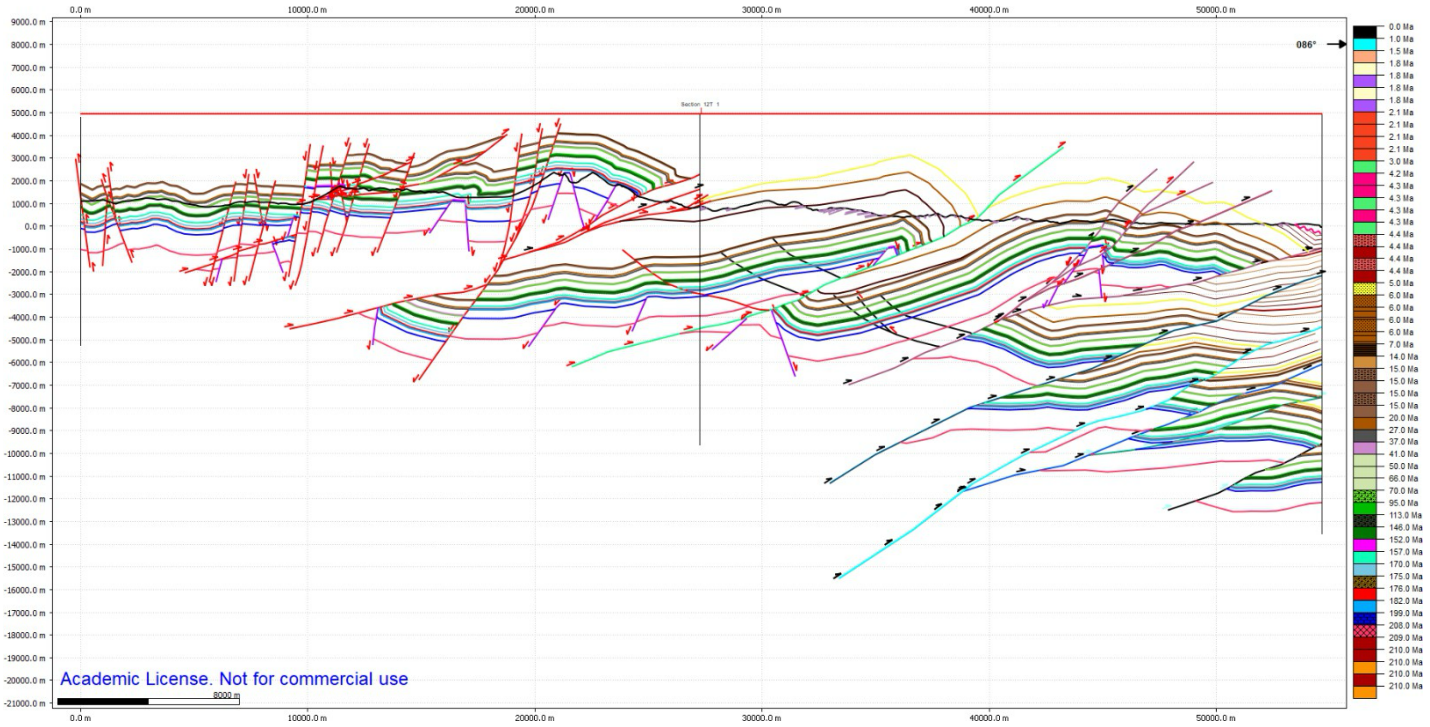

Figure S14. Cross section S12.

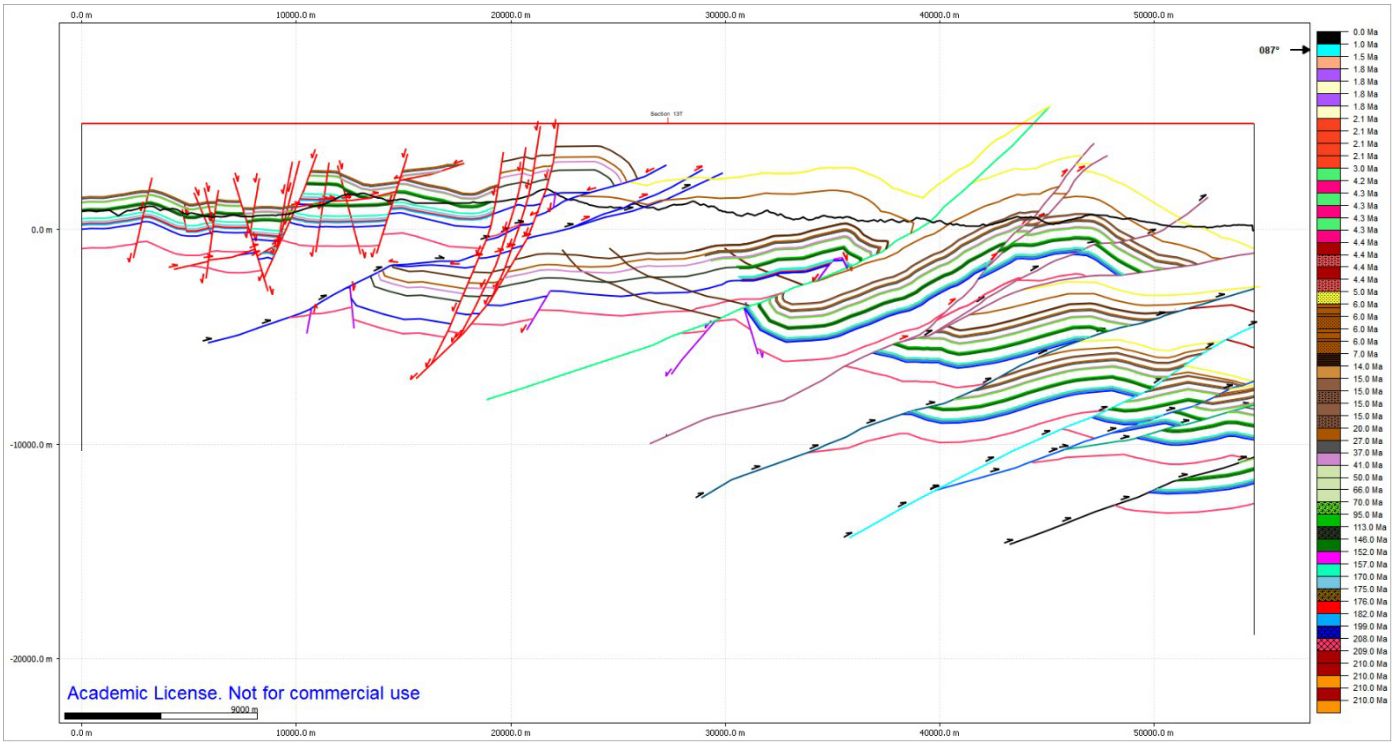

Figure S15. Cross section S13.

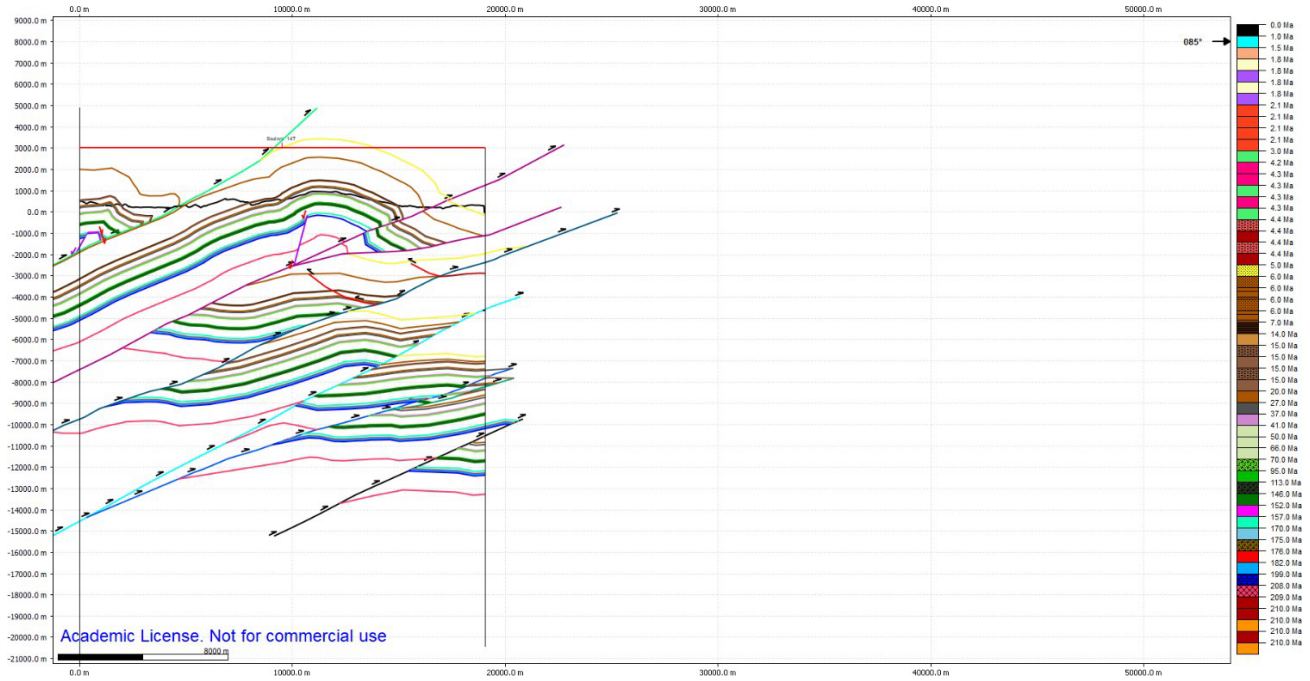

Figure S16. Cross section S14.

Text S1. DEXP and SCALFUN methods

Following the formulation of Fedi (2007), consider any n-order vertical derivative of the Newtonian potential of a pole source at Q(x0, y0, z0 < 0), evaluated at points x = x0, y = y0, z > 0:

$$f_n(z) = \frac{1}{(z-z_0)^{n+1}} \qquad (1).$$

Because of field dilation with altitude, absolute values of the field reach maxima along straight ridges converging toward the source position, producing cone-like patterns in (x, z) space (Fig. S1, top). Fedi (2007) introduced the scaling function τn:

$$\tau_n = \frac{\partial \log f_n}{\partial \log z} = -\frac{S_n z}{z-z_0} \qquad (2),$$

where Sn is the structural index, defined as the opposite of the homogeneity degree (n + 1). The DEXP transformation of order n is defined as:

$$W_n(z) = z^{\alpha_n} f_n(z) \qquad (3),$$

where αn = Sn/2 is the scaling exponent. A key property of the DEXP transformation is that Wn exhibits meaningful extreme points at z = -z0 for a given source depth z0, enabling depth estimation. DEXP assumes that real sources can be approximated by semi-infinite solids or volume-less figures and grouped into simple morphological classes.

In this framework, spherical sources can be approximated by point sources at their center; vertically or horizontally elongated sources (e.g., ridges, paleovalleys, tunnels, volcanic necks) can be approximated by line sources; and planar sources (e.g., sills, dikes, thrust-related steps) can be approximated by plane models. These may be treated as one-point sources in the sense of Stavrev (1997), where the model is parameterized by the coordinates of a single point representing the source (center, edge, or vertex depending on morphology). Equation (2) can be rewritten by setting z =

1/q, making τn a function of q:

$$\tau_n(q) = -\frac{S_n}{1-z_0 q} \quad (4).$$

which yields the property (Fedi, 2007):

$$\tau_n\,(q \rightarrow 0) = -S_n \quad (5).$$

Accordingly, the intercept of τ_n versus q provides an estimate of S_n (Fig. S1, bottom), which does not depend on z_0. Because the altitude zero-level is arbitrary, altitudes can be rescaled, and for any guessed depth $\bar{z}_0$ the rescaled scaling function:

$$\tau_n(q, \hat{z}_0) = -\frac{S_n(1-\hat{z}_0 q)}{1-z_0 q} \quad (6)$$

will be increasing, decreasing, or constant with q for $\bar{z}_0$ greater than, lower than, or equal to the true z_0, respectively. Thus, source depth may be estimated by identifying the $\bar{z}_0$ value that produces a zero slope in the rescaled scaling function.

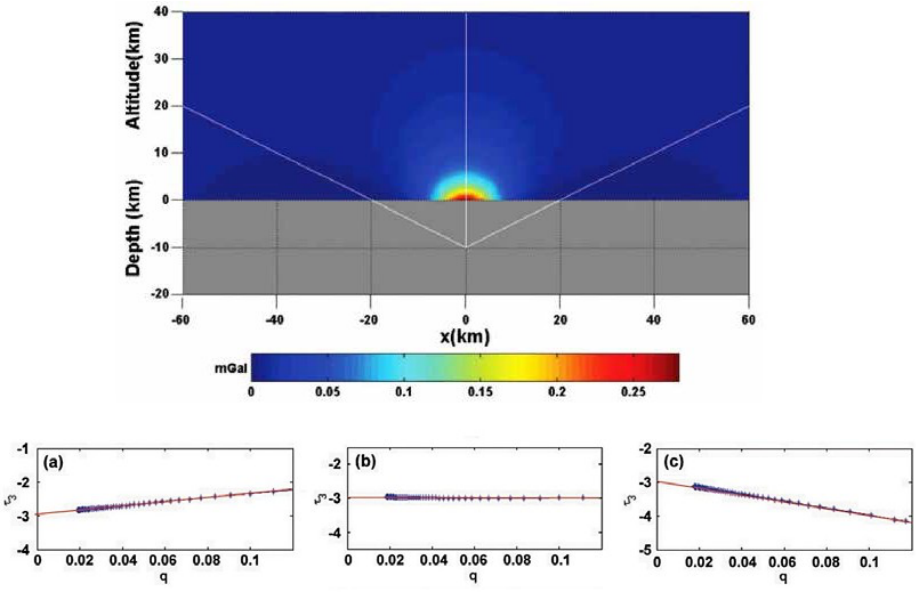

Figure S17. DEXP and SCALFUN method and scaling-function behavior. Top: Vertical section of the upward-continued field generated by a spherical source with radius of 1 km, depth of 10 km, and density contrast of 1 g/cm³. Straight lines defined by field maxima are shown as white solid lines and referred to as ridges. Because potential fields broaden upward with increasing continuation level, the ridges converge toward the source position and form cone-like structures. Bottom: Scale function used to determine the structural index.

Text S2. Crustal geothermal model: inputs, workflow, and assumptions

Objective and rationale

A steady-state, one-dimensional conductive thermal model was implemented to reconstruct vertical geotherms along the main west–east crustal transect. The procedure follows the analytical approach adopted by Santini et al. (2021) for the Marche region, in which temperature–depth profiles are calculated from surface temperature, mantle heat flow, layer thicknesses, thermal conductivity, and radiogenic heat production assigned to the main sedimentary and crustal units. This approach was adopted because direct borehole constraints on geothermal gradients are not available within the study area at the depths required to constrain the seismogenic layer. The model therefore provides an internally consistent first-order estimate of the crustal thermal structure that can be integrated with the gravity-constrained geological section and earthquake hypocenter distribution. Vertical geotherms were calculated for 42 sampling points, hereafter referred to as pseudo-wells, distributed at regular 2 km spacing along the crustal transect.

Geometrical framework and model parameterization

All geometrical inputs were derived from the crustal-scale geological cross-section developed in this study. Moho depth and intracrustal layering follow the gravity-constrained density model used to construct and validate the transect geometry. Surface elevation along the transect was extracted from the digital elevation model used in the main manuscript and was adopted as the upper boundary of each pseudo-well. For each pseudo-well, the input geometry includes: (i) surface elevation, (ii) modeled Moho depth, (iii) depths of the main stratigraphic and crustal horizon tops, and (iv) the corresponding layer thicknesses used in the thermal calculations. The modeled lithological column was simplified into the main stratigraphic and crustal units represented in the balanced cross-section, including the siliciclastic cover, marly units, carbonate multilayer, Calcare Massiccio, Burano Formation, metasedimentary basement, upper crust, middle crust, and lower crust. This simplified parameterization is appropriate for the scale of the model, because the objective is to estimate first-order crustal thermal gradients rather than local thermal perturbations associated with individual faults or fluid pathways.

Thermal properties and input dataset

Thermal conductivity and radiogenic heat production values were assigned to each lithological and crustal unit using representative values from previous thermal and rheological studies of the Apennines and continental crust. The adopted workflow and thermal parameterization are primarily based on Santini et al. (2021), with additional constraints from regional heat-flow modeling and crustal thermal studies in the northern-central Apennines and central Italy, including Pauselli et al. (2019), Mancinelli et al. (2019), and related published compilations of crustal thermal properties. Frictional and viscous flow-law parameters were assigned from commonly used lithology-dependent rheological laws for sedimentary rocks, carbonates, evaporite-bearing units, phyllitic metasediments, and granitic to granulitic crustal domains, following standard experimental and modeling references

such as Brace and Kohlstedt (1980), Ranalli (1995), Burov (2011), and Santini et al. (2021). Input parameters are summarized in Table S2. For each pseudo-well and each horizon top, the dataset includes the pseudo-

well name, measured depth to the horizon top, horizon name, thermal conductivity k, radiogenic heat production H, and mantle heat flow Qm. Mantle heat flow was allowed to vary laterally between pseudo-wells, following the approach of Santini et al. (2021), to account for regional variations in crustal thickness and thermal regime. A constant surface temperature Ts = 13 °C was imposed for all pseudo-wells. Radiogenic heat production within the basement and crustal domain was assumed to decrease exponentially with depth, with a characteristic scale depth D = 10 km.

Table S2. Thermo-rheological parameters used for geothermal and rheological modeling. Thermal conductivity, radiogenic heat production, friction coefficient, and viscous flow-law parameters were assigned to the main lithological and crustal units represented in the thermal model. Abbreviations: k, thermal conductivity; H, radiogenic heat production; μf, friction coefficient; A, pre-exponential flow-law constant; n, stress exponent; E, activation energy.

Unit	Lithology	k (W m^{-1} K^{-1})	H (μW m^{-3})	μf	A (Pa^{-n} s^{-1})	n	E (kJ mol^{-1})
Siliciclastic cover	Siliciclastic	2.0–2.2 (rep 2.1)	1.0–1.15 (rep 1.05)	0.6	1×10^{-28}	3	130
Marly units	Marly	2.3–2.4 (rep 2.35)	0.40–0.45 (rep 0.43)	0.6	5×10^{-30}	3	130
Carbonate multilayer	Carbonate	2.4	0.4	0.6	5×10^{-30}	3	130
Calcare Massiccio	Carbonate	2.5	0.3	0.6	1×10^{-30}	3	130
Burano Formation	Dolomitic/ anhydritic	2.0	0.3	0.6	1×10^{-30}	4	150
Metasedimentary basement	Phyllites	2.6	2.0	0.6	4×10^{-28}	4	154
Upper crust (b1)	Granitic	2.7	1.8	0.6	1×10^{-28}	4	186
Middle crust	Intermediate	2.8	0.8	0.6	3×10^{-27}	4	240
Lower crust	Granulitic	3.0	0.3	0.6	3×10^{-26}	4	276

Surface heat flow (Qs)

For each pseudo-well, surface heat flow was computed as the sum of mantle heat flow and the radiogenic contribution from the sedimentary cover and crystalline crust according to:

$$Q_s = Q_m + H_{CS}h_{CS} + H_B D \left[1 - \exp\left(-\frac{h_B}{D}\right)\right]$$

where Qs is surface heat flow, Qm is mantle heat flow, HCS is the mean radiogenic heat production of the sedimentary cover, hCS is the cover thickness from the surface to the top-basement marker, HB is the mean radiogenic heat production assigned to the basement and crustal domain below the top-basement marker, hB is the basement thickness from the top-basement marker to the Moho, and D is the characteristic depth scale for exponential radiogenic heat-production decay. Mean values of HCS and HB were derived consistently from the adopted layer aggregation in Table S1.

Temperature was computed incrementally from the surface downward, enforcing temperature continuity at each horizon top and using the thermal conductivity and radiogenic heat-production values assigned to each interval. For sedimentary-cover intervals, temperature at the base of a layer was computed from the temperature at its top as:

$$T(z) = T_{prev} + \left(\frac{Q_s}{k}\right)\Delta z - \left[\frac{H}{2k}\right](\Delta z)^2$$

where Tprev is temperature at the top of the interval, k is thermal conductivity, H is radiogenic heat production, and Δz is interval thickness.

For basement and deeper crustal layers, the conductive geotherm includes an exponentially decaying radiogenic term and uses Qm as the basal heat-flow contribution:

$$T(z) = T_{prev} + \left(\frac{Q_m}{k}\right)\Delta z + \left(H\frac{D^2}{k}\right)\left\{\exp\left[-\frac{z_{prev} - z_{b1}}{D}\right] - \exp\left[-\frac{z - z_{b1}}{D}\right]\right\}$$

where zprev and z are the depths from the surface at the top and base of the interval, respectively, and zb1 is the depth to the top-basement marker, used as the reference level for the onset of radiogenic decay in the basement and crustal domain.

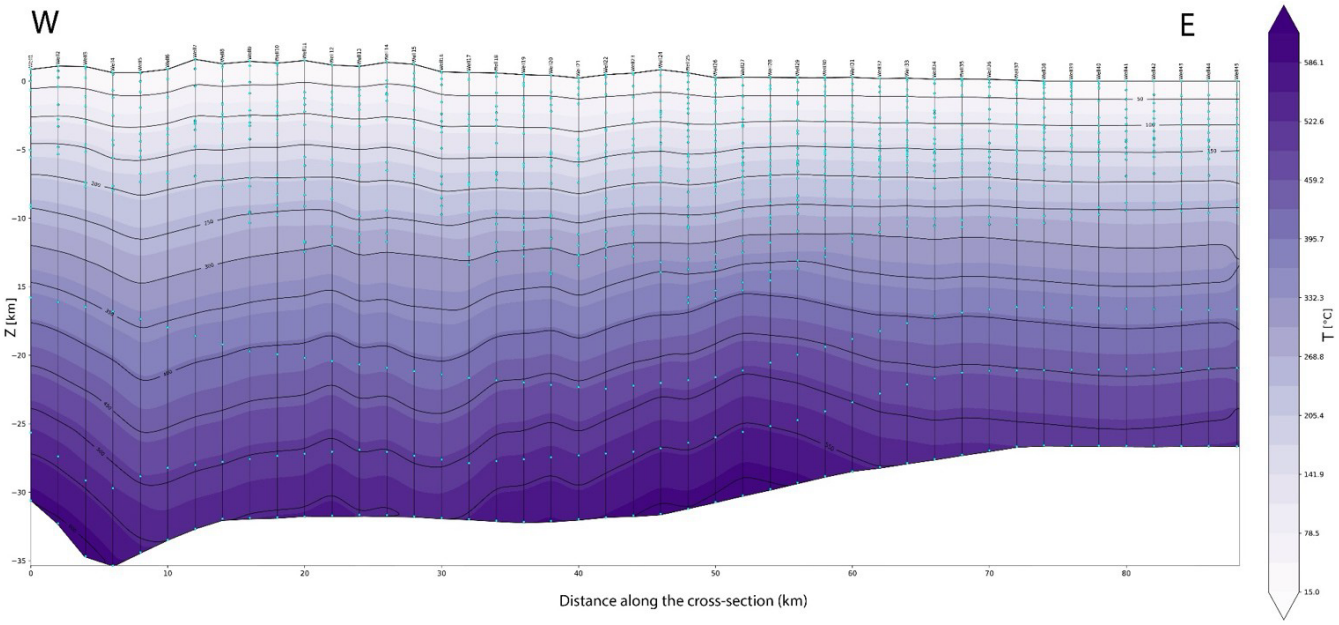

Figure S18. Crustal-scale thermal model along the studied transect. The model shows the distribution of calculated temperatures along the gravity-constrained crustal section used in this study. Isotherms were obtained by interpolating one-dimensional conductive geotherms calculated at 42 pseudo-wells distributed at regular spacing along the transect.

Assumptions and limitations

The model assumes steady-state conductive conditions and does not include transient effects, advective heat transport, or localized thermal perturbations associated with fluid circulation along faults (Figure S18). This simplification is justified by the crustal scale of the study and by the lack of deep borehole temperature data within the investigated area. The model is therefore intended as a first-order thermal framework rather than a high-resolution geothermal reconstruction. Model accuracy primarily depends on the representativeness of the thermal parameters assigned to each unit and on the robustness of the Moho depth and crustal geometry derived from the gravity-constrained transect.

References

Brace, W. F., & Kohlstedt, D. L. (1980). Limits on lithospheric stress imposed by laboratory experiments. Journal of Geophysical Research: Solid Earth, 85(B11), 6248–6252. https://doi.org/10.1029/JB085iB11p06248

Burov, E. B. (2011). Rheology and strength of the lithosphere. Marine and Petroleum Geology, 28(8), 1402–1443. https://doi.org/10.1016/j.marpetgeo.2011.05.008

Mancinelli, P., Porreca, M., Pauselli, C., Minelli, G., Barchi, M. R., & Speranza, F. (2019). Gravity and magnetic modelling of Central Italy: Insights into the depth extent of the seismogenic layer. Geochemistry, Geophysics, Geosystems, 20. https://doi.org/10.1029/2018GC008002

Pauselli, C., Gola, G., Mancinelli, P., Trumpy, E., Saccone, M., Manzella, A., & Ranalli, G. (2019). A new surface heat flow map of the Northern Apennines between latitudes 42.5 and 44.5 N. Geothermics, 81, 39–52. https://doi.org/10.1016/j.geothermics.2019.04.002

Ranalli, G. (1995). Rheology of the Earth (2nd ed.). Chapman & Hall.

Santini, S., Basilici, M., Invernizzi, C., Jablonska, D., Mazzoli, S., Megna, A., & Pierantoni, P. P. (2021). Controls of radiogenic heat and Moho geometry on the thermal setting of the Marche Region (Central Italy): An analytical 3D geothermal model. Energies, 14, 6511. https://doi.org/10.3390/en14206511